PCCP

Accepted Manuscript

ROYAL SOCIETY OF CHEMISTRY

www.rsc.org/pccp

Performance of polarisation functionals for linear and nonlinear optical properties of bulk zinc chalcogenides ZnX (X=S,Se,Te).

M. Grüning,[*a,d] **C. Attaccalite,**[b,c,d]

Received Xth XXXXXXXXXX 20XX, Accepted Xth XXXXXXXXX 20XX
First published on the web Xth XXXXXXXXXX 20XX
DOI: 10.1039/b000000x

Abstract

We calculated the frequency dependent macroscopic dielectric function and second-harmonic generation of cubic ZnS, ZnSe and ZnTe within time-dependent density-polarisation functional theory. The macroscopic dielectric function is calculated in a linear response framework, second-harmonic generation in a real-time framework. The macroscopic exchange-correlation electric field that enters in the time-dependent Kohn-Sham equations and accounts for long range correlation is approximated as a simple polarisation functional $\alpha\mathbf{P}$ where $\mathbf{P}$ is the macroscopic polarisation. Expressions for α are taken from the recent literature. The performance of the resulting approximations for the exchange-correlation electric field is analysed by comparing the theoretical spectra with experimental results and results obtained at the level of the independent particle and the random-phase approximation. For the dielectric function we also compare with state-of-the art calculations at the level of the Bethe-Salpeter equation.

1 Introduction

At present, one of the most successful approaches to treat optical excitations in finite gap crystals is the GW+Bethe–Salpeter equation (GW+BSE) on top of density-functional theory (DFT).[1] In this approach the Kohn-Sham (KS) eigensolutions $\{\phi_n, \varepsilon_n\}$ are perturbatively corrected within the GW approximation and used as a basis to expand the BSE which reads schematically:

$$L = L_0 + L_0 \Xi L. \tag{1}$$

The latter is a Dyson equation for the electron-hole correlation function L. The first term, L_0 is the independent two-particles Green's function given by the product of two single-particle Green's function. Ξ is the Bethe-Salpeter kernel and contains the long-range correlation in the form of screened electron-hole attraction which is the key ingredient to describe optical excitations in finite-gap crystals.[2] Without this term excitation wavefunctions are described by KS-particle products $\phi_v(\mathbf{r})\phi_c(\mathbf{r}')$ (v stands for valence, c for conduction): if the hole is at $\phi_v(\mathbf{r})\delta(\mathbf{r}-\mathbf{r}_h)$, the electron $\phi_c(\mathbf{r}')$ is delocalised over the whole crystal. This is in stark contrast with what is observed in finite gap crystals where the optically excited electron is localised around the hole. For example, the Frenkel exciton in bulk LiF—a large gap insulator—is delocalised within 2-3 unit cells.[3] Frenkel excitons, and excitons in general, are well captured within the GW+BSE. Unfortunately, Ξ is computationally expensive so that calculations become quickly awkward with the system size. It is thus desirable to look for alternatives, as for example time-dependent-DFT (TD-DFT).

Within the linear response, TD-DFT is formulated as a Dyson equation for the density-response function[4] $\chi^{\rho\rho}$

$$\chi^{\rho\rho} = \chi_0^{\rho\rho} + \chi_0^{\rho\rho} f_{\mathrm{Hxc}} \chi^{\rho\rho}, \tag{2}$$

with analogous ingredients to Eq. (1), the independent particles density-response function χ_0 and the kernel f_{Hxc}, a functional of the electron density which should introduce correlation. In practice standard approximations[5] for the exchange-correlation part of the kernel f_{xc} are missing the long-range correlation essential for describing excitonic effects[6]. In practice optical spectra of finite gap crystals within standard TDDFT are very similar to those obtained within the Random-Phase approximation (Eq. (2) with $f_{\mathrm{xc}} = 0$, that is only the mean-field part of the kernel is included).

The development of f_{xc} kernels able to treat optical excitations in finite gap crystals is ongoing and progresses have been made in recent years. The works of Marini et al[7], and of Sottile et al.[8] proposed a successful approximation by "rewriting" the GW+BSE [Eq. (1)] within the TD-DFT framework. This approximation shares with the GW+BSE not only the accuracy, but also the computational cost, and it is therefore referred as a proof of principle rather than routinely employed in "real-world" applications. From the BS kernel were derived simplified approximations[9–11] with the same long-range behaviour, which is essential to describe excitonic effects. These approximations work quite well for semiconductors, but tend to overestimate the absorption at bound exciton resonances in large gap insulators. In addition they employed empirical parameters. The (revised) bootstrap kernel[12,13] and the jellium with gap model kernel[14] have the correct long-range behaviour as well with the advantage of being first-principles approaches. A common denominator of the these approximations for the kernel is that there is no corresponding exchange-correlation potential from which they can be derived. In fact, kernels with the correct long-range behaviour can be derived from the macroscopic exchange-correlation electric field[15–17], which is a functional of the macroscopic polarisation and electronic density rather than of the electronic density alone. Starting from TD-current-density functional theory (TD-CDFT), Berger[17] derived a parameter-free kernel, functional of the polarisation, with the correct long-range behaviour which reproduces well the optical spectra of semiconductors, insulators and metals.

In this work we calculate the frequency dependent macroscopic dielectric function and the second harmonic generation (SHG) spectra of bulk ZnX (X=S,Se,Te) within a TD-density polarisation functional theory (TD-DPFT) in which both the electronic density and macroscopic polarisation are basic variables (Sec. 2). Calculations are carried out both within a linear response and a real-time framework (Sec. 3). The discussion and analysis of the results (Sec. 4) focus on the performance of the polarisation functionals—derived from the above-discussed kernels with the correct long-range behaviour. The performance is compared with results at the independent particle and random-phase approximation (RPA) level and measured against the experimental spectra[18–22] and for the dielectric function against state-of-the-art calculations at the Bethe-Salpeter equation level. Because of the technology relevance of bulk zinc chalcogenides, abundant literature is available on first-principles calculations of both linear and nonlinear optical properties[23–30] of those systems. Those calculations are all performed at the independent particle level and with few exceptions[30] neglecting the spin-orbit coupling. In addition of analysing the performance of the polarisation functional approximations then, the calculations here presented elucidate the role of crystal-field effects and electron-hole interaction in these systems. The latter has been argued to be key in explaining the large difference observed between the measured SH intensity and model results.[18]

2 Theory

We consider a periodic crystal with a finite gap with volume Ω in a (time-dependent) macroscopic electric field $\mathcal{E}$. The external energy reads

$$E^{\rm ext}[n,\mathbf{P}] = \int_\Omega n(\mathbf{r})v_{\rm ext}(\mathbf{r})\,d\mathbf{r} - \Omega\mathcal{E}\cdot\mathbf{P}, \qquad (3)$$

where $v_{\rm ext}$ is the microscopic external potential, $n(\mathbf{r})$ the electronic density and $\mathbf{P}$ the macroscopic polarisation. When $\mathcal{E}=0$ the evolution of the system is fully described by the density which following the Runge–Gross theorem has a one-to-one correspondence with the microscopic external potential.

When $\mathcal{E}\neq 0$, the density alone is not sufficient anymore,[31–34] and the correct framework to describe the evolution of the system is TD-CDFT.[35,36] Alternatively, for finite-gap crystals one can choose the density and the macroscopic polarisation[37] as key variables (for the static case see Martin and Ortiz[34]):

$$(n,\mathbf{P}) \leftrightarrow (v_{\rm ext},\mathcal{E}).$$

In fact from the polarisation $\mathbf{p}(\mathbf{r},t)$ one can determine the current $\mathbf{j}(\mathbf{r},t)$ at each t

$$\mathbf{j}(\mathbf{r},t) = \frac{\partial\mathbf{p}(\mathbf{r},t)}{\partial t}. \qquad (4)$$

Then, $\mathbf{p}$ and $\mathbf{j}$ are equivalent in the sense that they can both be employed as basic variable. Furthermore the density and the microscopic, longitudinal components of $\mathbf{p}$ can be used equivalently by virtue of the continuity equation:

$$\nabla\cdot\mathbf{p}(\mathbf{r};t) = -n(\mathbf{r};t). \qquad (5)$$

As in the $\mathcal{E}=0$ case we can define a Kohn-Sham system whose density (in all the following we assume spin-unpolarised systems, but equations can be straightforwardly generalised to the spin polarised and noncollinear case)

$$n^s(\mathbf{r},t) = 2\sum^{\rm occ}|\phi_{n\mathbf{k}}(\mathbf{r};t)|^2 \qquad (6)$$

and macroscopic polarisation (in the α cartesian direction) defined as a Berry phase

$$P^s_\alpha = -\frac{2ie}{(2\pi)^3}\sum_n^{\rm occ}\int d\mathbf{k}\langle u_{\mathbf{k}n}|\partial_{k_\alpha}u_{\mathbf{k}n}\rangle. \qquad (7)$$

should reproduce both the density and macroscopic polarisation of the physical system, i.e. $n=n^s$ and $\mathbf{P}=\mathbf{P}^s$. The periodic part $u_{n\mathbf{k}}$ of the Bloch states $\phi_{n\mathbf{k}}(\mathbf{r},t) = \exp(i\mathbf{k}\mathbf{r})u_{n\mathbf{k}}(\mathbf{r};t)$ is the solution of the time-dependent Kohn-Sham equations

$$i\partial_t u_{n\mathbf{k}} = \left(H^{s,0}_{\mathbf{k}} + \Delta v^{\rm Hxc}(\mathbf{r},t) - \Omega\,\mathcal{E}^s(t)\cdot\partial_{\mathbf{k}}\right)u_{n\mathbf{k}}. \qquad (8)$$

In Eq. (8), $H^{s,0}_{\mathbf{k}}$ is the ground-state zero-field KS Hamiltonian, $\Delta v^{\rm Hxc}$ is the change in the microscopic effective potential due to the changes in the microscopic Hartree $v_H[n]$ and exchange-correlation potential $v_{\rm xc}[n,\mathbf{P}]$. $\mathcal{E}_s$ is the macroscopic effective electric field that is the sum of the macroscopic external electric field, the induced field and the exchange-correlation electric field

$$\mathcal{E}^s[n,\mathbf{P}] = \mathcal{E}^{\rm ext} + \mathcal{E}^{\rm ind}[\mathbf{P}] + \mathcal{E}^{\rm xc}[n,\mathbf{P}]. \qquad (9)$$

$v_{\rm xc}[n,\mathbf{P}]$ and $\mathscr{E}_{\rm xc}[n,\mathbf{P}]$ guarantee that the density and macroscopic polarisation of Kohn-Sham and physical systems are equal. In practice both need to be approximated.

In what follow we derive approximations for $\mathscr{E}_{\rm xc}[n,\mathbf{P}]$ from long-range corrected approximations for the exchange-correlation kernel proposed in the literature. Within linear response TD-DFT the kernel $f^{\rm xc}(\mathbf{r},\mathbf{r}';t-t')$ describes how the exchange-correlation potential changes following a perturbation of the density. In analogy, we can define a kernel tensor $\bar{F}^{\rm xc}(\mathbf{r},\mathbf{r}';t-t')$ that describes how the exchange-correlation macroscopic field changes following a perturbation of the macroscopic polarisation and the density. In reciprocal space (see also Maitra and coworkers[35])

$$\mathscr{E}_{\rm xc}(t) = \int dt' \Big[\bar{F}^{\rm XC}_{00}(t-t')\mathbf{P}(t') - i\sum_{\mathbf{G}'\neq 0} \bar{F}^{\rm XC}_{0\mathbf{G}'}(t-t')\frac{n'_{\mathbf{G}}(t')}{\mathrm{G}'^2}\mathbf{G}'\Big]. \tag{10}$$

The relation between $\bar{F}^{\rm XC}$ and $f^{\rm XC}$ is found from the relation between the corresponding response functions (density and polarisation):

$$f^{\rm XC}_{\mathbf{G}\mathbf{G}'}(\mathbf{q};t-t') = \frac{\bar{F}^{\rm XC}_{\mathbf{G}\mathbf{G}'}(\mathbf{q};t-t')\cdot\bar{g}}{|\mathbf{q}+\mathbf{G}||\mathbf{q}+\mathbf{G}'|}, \tag{11}$$

where $\bar{g}$ is the metric tensor. When comparing Eq. (11) with the general expression for the long-range corrected approximation for the kernel ($\alpha > 0$)

$$f^{\rm LRC}_{\rm XC}(\mathbf{q}\to 0;t-t') = \lim_{\mathbf{q}\to 0} -\frac{\alpha}{|\mathbf{q}|^2}\delta(t-t'), \tag{12}$$

one obtains (for cubic systems where $\bar{g}=\bar{I}$, the identity tensor)

$$\bar{F}^{\rm XC}_{0\mathbf{G}}(\mathbf{q}=0,t-t') = -\alpha(\mathbf{G};t)\bar{I}\delta(t-t'), \tag{13}$$

and therefore

$$\mathscr{E}_{\rm xc}(t) = -\alpha(0;t)\mathbf{P}(t) + i\sum_{\mathbf{G}\neq 0}\alpha(\mathbf{G};t)\frac{n_{\mathbf{G}}(t)}{\mathrm{G}^2}\mathbf{G}. \tag{14}$$

In this work we consider the following approximations for α:

1. An empirical expression derived by Botti and coworkers[10] from the fit of the optimal α for the absorption spectrum of several semiconductors versus the macroscopic static dielectric function $\varepsilon_M(0)$:

   $$\alpha^{\rm EMP} = A\varepsilon_M^{-1}(0) + B \tag{15}$$

   with $A = 4.615$ and $B = 0.213$ and $\varepsilon_M(0)$ evaluated at the quasiparticle level.

2. An energy dependent expression derived from a single Lorentz oscillator model with plasmon frequency ω_p and resonance frequency ω_g corresponding to the average absorption gap of the material:[11]

   $$\alpha^{\rm ED}(\omega) = C\left(\alpha_0 + \beta\omega^2\right) \tag{16}$$

   $$\alpha_0 = \frac{\omega_g}{\varepsilon_M(0)\omega_p^2},\ \beta = \frac{\alpha_0}{\omega_g^2} \tag{17}$$

   with $C = 104.5$ found empirically again by fitting optimal α values for several materials.

3. The static part of the polarisation functional derived from a simple model for a bound exciton by Berger[17]

   $$\alpha^{\rm BER} = \frac{1}{\chi^{\rm RPA}\varepsilon_M^{\rm RPA}(0)} \tag{18}$$

   with $\varepsilon_M^{\rm RPA}(0)$ calculated at the RPA level. This expression for α is the same (but for the choice of the approximation of $\varepsilon_M(0)$) as the one in the revised bootstrap kernel[13] that is thus not (explicitly) included in the present analysis.

4. The expression derived by Trevisanutto and coworkers[14] from the jellium with gap model (JGM),

   $$\alpha^{\rm JGM}(\mathbf{r};t) = 4\pi\tilde{B}\left[1-\exp\left(-\frac{E_{\rm gap}^2}{4\pi n\tilde{B}}\right)\right]. \tag{19}$$

   with $\tilde{B} = (B+E_{\rm gap})/(1+E_{\rm gap})$, where $B = B[n]$ is a functional of the density found by fitting the local field factor of the homogeneous electron gas from Quantum Montecarlo data.[38] The band gap, $E_{\rm gap}$, is the indirect gap of the material.

Note that the expressions in Eqs. (15)–(18) approximate only $\alpha(0;t)$ in Eq. (14), and the microscopic contribution from $\alpha(\mathbf{G};t)$ is assumed to be negligible. Instead, in the JGM approximation [Eq.(19)], the cell average of $\alpha^{\rm JGM}(\mathbf{r};t)$ gives $\alpha(0;t)$ and the Fourier transform $\alpha(\mathbf{G}\neq 0;t)$ in Eq. (14). Furthermore $\alpha^{\rm JGM}$ depends on time through the density, contrary to Eq. (15),(18) which are time-independent. The energy dependent expression [Eq. (16)] can be in principle Fourier transformed into a time-dependent expression, though the particular expression for the transformation is not straightforward.

3 Implementation and computational details

The macroscopic dielectric functions have been calculated within the linear response framework using Yambo.[39] The first order susceptibility χ within the DPFT is calculated as[17,40]

$$\chi = \frac{\chi^0}{1-\alpha\chi^0} \tag{20}$$

In Eq. (20), χ^0 is the first order susceptibility and is obtained from the microscopic density response function [Eq. (2)] within the random-phase-approximation (RPA), that is by neglecting the exchange-correlation part in the f_{Hxc}. For α we use the approximations described in the previous Section. In the JGM approximation we only consider the $\mathbf{G} = 0$ term.

The SHG spectra have been calculated within the real-time DPFT approach in Eqs. (6)–(9) which has been implemented in a development version of Yambo.[39,41] The TD-KS states are expanded in the basis of the ground-state zero-field KS eigenfunctions $\phi^0_{n\mathbf{k}}(\mathbf{r},t) = \exp(i\mathbf{kr})u^0_{n\mathbf{k}}(\mathbf{r})$. In such basis the equations of motion [Eq. (8)] read,

$$i\dot{c}_{mn\mathbf{k}} = \left(\varepsilon_{l\mathbf{k}}\delta_{ml} + \Delta v^{\mathrm{Hxc}}_{ml\mathbf{k}} - \xi_{ml\mathbf{k}}\right) c_{ln\mathbf{k}}, \qquad (21)$$

where $c_{mn\mathbf{k}} = \langle u^0_{m\mathbf{k}}|u_{n\mathbf{k}}\rangle$, $\varepsilon_{l\mathbf{k}}$ are the eigenenergies of the ground-state, zero-field crystal Hamiltonian $H^{s,0}_{\mathbf{k}}$, $\Delta v^{\mathrm{Hxc}}_{ml\mathbf{k}} = \langle u^0_{m\mathbf{k}}|\Delta v^{\mathrm{Hxc}}|u^0_{l\mathbf{k}}\rangle$ and $\xi_{ml\mathbf{k}}$ is the field coupling operator. Following the works of Souza et al.[42] and of Nunes and Gonze[43] we approximate the (Gauge covariant) $\mathbf{k}$-derivative in Eq. (8) with a finite difference five-point midpoint formula. Note that the long-range correlation effect enters in the field coupling operator. For α we considered α^{BER}, α^{ED} and α^{JGM} (considering the $\mathbf{G} = 0$ and the $\mathbf{G} \neq 0$ terms). The equations of motion [Eq. (21)] have been integrated using Crank-Nicholson method.[44] The second harmonic spectra have been obtained from $\mathbf{P}(t)$ [Eq. (7)] by Fourier inversion.[41]

We performed ground state DFT calculation with the Perdew Burke Ernzerhof[45] approximation for the exchange-correlation energy functional using the planewave pseudopotential PWscf[46] code. Troullier-Martins normconserving pseudopotentials[47] have been generated with the ld1 atomic code in the Quantum Espresso suite[48] from the pslibrary pseudopotential input library.[49] We generated scalar relativistic pseudopotential and full-relativistic pseudopotentials for Zn, Se and Te in ZnSe and ZnTe. Within the linear response framework for ZnSe and ZnTe we performed spin-noncollinear calculations with spin-orbit interaction. For the self-consistent calculation of the density we employed a $10 \times 10 \times 10$ Monkhorst-Pack[50] mesh in reciprocal space and a planewave cutoff of 80 Ry at the experimental lattice constant (5.41Å, 5.67Åand 6.09Å respectively for ZnS, ZnSe and ZnTe)[20–22]. The KS eigensolutions needed in Eq. (21) are obtained from a non-self consistent calculations on a $18 \times 18 \times 18$ Monkhorst-Pack[50] mesh. We include bands 2 to bands 13 and bands 3 to bands 26 for spin-unpolarised and spin-noncollinear calculations respectively. In the solution of the Bethe-Salpeter equation [Eq. 1] we used a double-grid approach with a $8 \times 8 \times 8$ mesh in reciprocal space as coarse grid plus a shifted $24 \times 24 \times 24$ auxiliary mesh.[51] For the screened exchange part of the Bethe-Salpeter kernel in the calculation of the static RPA response we employed 40 bands in the summation over bands and a cut-off of 3 Ha (ZnS), 3.3 Ha (ZnSe) and 3.6 Ha (ZnTe) for the summation over reciprocal lattice vectors. Calculations at this level of theory do not include spin-orbit coupling.

As the screened exchange kernel in the Bethe-Salpeter equation and $\mathscr{E}^{\mathrm{xc}}$ in DFPT account for the excitonic effects, but not for the underestimated absorption edge position, the KS eigenenergies in Eq. (21) are corrected so to reproduce the experimental bandgap at Γ of 3.80 eV, 2.80 eV and 2.38 eV for ZnS, ZnSe and ZnTe[20–22]: a rigid shift of 1.80 eV, 1.65 eV (1.51 eV) and 1.62 eV (1.30 eV) is applied respectively (in parentheses scissor operator for spin unpolarised calculations). Finally for all the systems we introduce a Lorentzian broadening of 0.2 eV to simulate dephasing effects.

4 Results

4.1 Macroscopic dielectric function

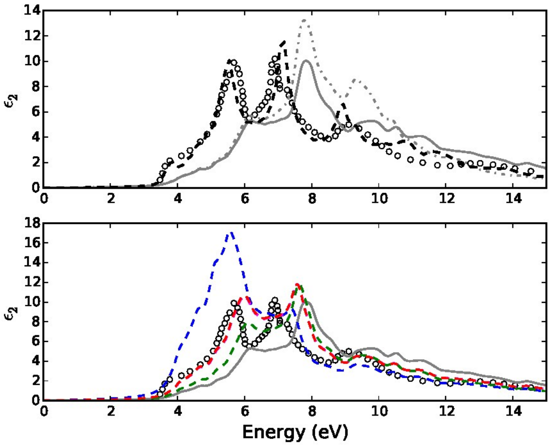

Fig. 1 Optical absorption (imaginary part of the macroscopic dielectric function ε_2) in bulk ZnS. Top panel: experimental spectrum[19](circles) compared with the independent particle (grey dashed-dotted line) and random phase approximation (grey continuous line) and Bethe-Salpeter equation (black dashed line). Bottom panel: experimental spectrum (circles) compared with the approximations for the polarisation functional described in Sec. 2, $\alpha^{\mathrm{EMP}}\mathbf{P}$ (red dashed line), $\alpha^{\mathrm{BER}}\mathbf{P}$ (magenta dashed line), $\alpha^{\mathrm{ED}}\mathbf{P}$ (green dashed line) and $\alpha^{\mathrm{JGM}}\mathbf{P}$ (blue dashed line). For reference the random phase approximation is also shown (grey continuous line).

The top panel of Fig. 1 shows the experimental optical absorption spectrum of ZnS[19] —the imaginary part of the macroscopic dielectric function ε_2— measured at room temperature. The absorption edge (E_0) is at 3.7 eV followed by three peaks at 5.7 eV (E_1), 7.0 eV (E_2) and 9.1 eV (E'_1) and a shoulder ($E_2 + \delta$) at 7.95 eV. In the same panel we plotted the spectra calculated within the independent particle approximation [only first term in Eqs. (2)], the RPA [with $f_{\mathrm{xc}} = 0$ in

Approximation	ZnS	ZnSe	ZnTe
α^{BER}	0.75	0.53	0.34
α^{JGM}	1.34	0.87	0.75
α^{ED}	0.26	0.24	0.20
α^{EMP}	0.78	0.64	0.49

Table 1 Calculated values of α for the approximations described in Sec. 2, Eqs. (15)–(19)

Eq. (2)] and the Bethe-Salpeter Equation. In both cases the KS energies were corrected with a scissor operator of 1.8 eV to match the experimental bandgap. All the experimental features are recognisable in the independent particle spectrum, but with large errors in their position, shape and intensity: the absorption edge is far less pronounced than in the experiment, E_1 appears as a shoulder and it is blue shifted by 0.3 eV, the E_2 and E'_1 peaks are overestimated and blue-shifted by 0.3 eV as well. With respect to the independent particle approximation, the RPA corresponds to adding crystal local-field effects. The latter do not affect either the absorption edge and E_1, but correct the overestimation of the E_2 and E'_1, though they do not change their position. Even if not plotted, addition of microscopic exchange-correlation effects (either in the form of a kernel within the linear response framework, or of a time-dependent potential within the real-time framework) does not result in significant changes with respect to the RPA spectra.[1]

The introduction of electron-hole attraction accounts for most of the observed differences between the independent particle/RPA spectra and the experimental curve: the spectrum obtained by solving the Bethe-Salpeter equation reproduces well both peaks position and intensities. Specifically, at the absorption edge (E_0) where the intensity of the independent particle/RPA spectra is underestimated the Bethe-Salpeter shows an exciton corresponding to a transition from the top valence to the bottom conduction band at the Γ point of the Brillouin zone and localised on the sulphur atom. Similarly the E_1 peak that in both independent particle/RPA calculations appears as a shoulder is clearly pronounced and has an intensity similar to the E_2 peak in agreement with what observed experimentally. Lastly, the blue shift of the energy of the E_1, E_2 and E'_1 peaks is also corrected by the introduction of the electron-hole attraction.[52]

The bottom panel of Fig. 1 compares the experimental optical absorption spectrum with theoretical spectra obtained by TD-DPFT with the approximations for the polarisation functional described in Sec. 2. Table 1 lists the values for α obtained in the different approximations. With respect to the spectrum obtained in the RPA by increasing α the absorption edge (E_0) becomes more pronounced, the E_1 peak becomes more intense and is redshifted and the E'_1 is reduced and redshifted. The intensity of E_2 is slightly increased up to a certain value of α, and then it decreases. In all cases the peak is redshifted with respect to the RPA result. Even if providing general improvements over the RPA none of the approximations provides a fully satisfactory agreement with experiment especially when compared with results at the Bethe-Salpeter level of theory. In particular the E_0 exciton is too weak and the E_1, E_2 peaks are still blue shifted by about 0.3 eV and 0.5 eV. The best description of the experimental features is given by the approximation proposed by Berger, $\mathscr{E}^{\mathrm{xc}} \approx \alpha^{\mathrm{BER}}\mathbf{P}$, and the empirical approximation proposed by Botti and coworkers, $\mathscr{E}^{\mathrm{xc}} \approx \alpha^{\mathrm{EMP}}\mathbf{P}$. The energy dependent approximation, $\mathscr{E}^{\mathrm{xc}} \approx \alpha^{\mathrm{ED}}\mathbf{P}$, is "too weak" for low photon energies, while the JGM approximation overestimates by almost a factor 2 the intensity E_1 peak and underestimates instead the intensity of the E_2 and E'_1 peaks, though providing a better agreement for the peaks position.

The real part of the experimental macroscopic function of ZnS is shown in Fig. 2. Signatures of the features discussed in the absorption spectrum are visible at 3.7 eV, 5.7 eV, 7.0 eV and 9.1 eV. At the independent particle level the low part of the spectrum (static limit) is well reproduced. This is likely due to an almost exact cancellation between crystal local field effects, that reduces the value of the static dielectric function (see RPA results) and excitonic effects that enhances the value of the the static dielectric function (see polarisation functional results in the bottom panel). Other features in the experimental spectrum are not well captured by both the independent particle and the RPA (top panel). Similarly to what observed for the imaginary part, the introduction of electron-hole attraction within the Bethe-Salpeter equation framework substantially improves the agreement with the experiment. In general adding the polarisation functionals lead as well to a better overall agreement with respect to the RPA results (with the exception of the JGM approximation), but again results are not as good as those obtained by the Bethe-Salpeter equation.

The optical absorption spectra of cubic ZnSe and ZnTe (Figs. 3 and 4) show analogous features as those discussed for ZnS. An important difference though is the visible spin-orbit splitting of the E_1 peak of about 0.29 eV for ZnSe and 0.58 eV in ZnTe.[21,22] Substituting S with heavier elements of group 16 of the periodic table has as consequence of increasing the dielectric screening (experimental average value at room temperature are 5.1 for ZnS[20] 5.9 for ZnSe[21] and 6.9 for ZnTe[22]) and thus lower the band gap. For ZnSe the absorption edge (E_0) is at 2.8 eV, E_1 at about 4.8 eV ($E_1+\Delta_{\mathrm{SO}}$ at 5.1 eV), E_2 at 6.5 eV and E'_1 at 8.2 eV. For ZnTe the absorption edge (E_0) is at 2.3 eV, E_1 at about 3.8 eV ($E_1+\Delta_{\mathrm{SO}}$ at 4.3 eV), E_2 at 5.2 eV. The independent particle and RPA show the same shortcomings which were discussed for ZnS. Again the spectra calculated with the Bethe-Salpeter equation are in good agreement with the experiment improving both the peaks position and intensity when compared to the independent particle/RPA calculations. As well adding the polarisation functionals to the RPA improves in general the agreement though to a lesser extend than at the Bethe-Salpeter equation level. The best agreement with experiment is obtained using the empirical α^{EMP} in Eq. (15) followed by the α^{BER} [Eq.(18)] and by α^{ED} [Eq.(16)]. Regarding the spin-orbit splitting all these approximations, and the RPA give similar good results (0.3 eV for ZnSe and about 0.5 eV for ZnTe). For ZnSe, the three above mentioned polarisation functional correct also the ratio of the E_1 and $E_1+\Delta_{\text{SO}}$ intensities with respect to the RPA. Regarding the JGM approximation, α^{JGM} is too large and overcorrects the RPA results.

Figures 5 and 6 plot the real part of the macroscopic dielectric function of ZnSe and ZnTe respectively. Results follow similar trends as for ZnS. The independent particle approximation reasonably reproduces the low energy part of the spectra because of cancellation of excitonic and local fields effects. The agreement though worsens substantially at higher energies. Consistently with what observed above, the spectra obtained by Bethe-Salpeter equation show a good overall agreement with the experiment. The polarisation functionals with α modelled as a function of the static dielectric function (α^{ED},α^{BER} and α^{EMP}) improved the agreement with the experiment if compared with the RPA especially in the case of ZnSe, but again agreement is worse if compared with the Bathe-Salpeter equation.

As noted in the introduction, calculations of the dielectric function at the independent particle level for these materials have been reported already in the literature.[23,24,26–30] When compared with these results we found that our calculations at the same level of approximation are in good agreement on peaks position and intensity once the onset of the spectra are shifted so to coincide.[53] Regarding spin-orbit effects we do not observe the overall reduction of absorption reported by Karazhanov and coworkers:[30] even for ZnTe—for which we observe the strongest spin-orbit interaction—the main difference between spectra with and without spin-orbit interaction is the splitting of the E_1 peak discussed above.

In what follows we analyse the performance of the polarisation functional approximations along the S, Se, Te series by looking at two signatures of excitonic effects: the E_1/E_2 peak intensity ratio and the redshift of the peaks position with respect to the independent particle/RPA. Results for the E_1/E_2 peak intensity ratio in the absorption are summarised for the different level of theory in Fig. 7. Whereas the experimental value ranges between 0.9–1.0, the independent particle approximation gives values between 0.4–0.5, with the ratio increasing with the chacolgenide atomic number. The underestimation is due to the underestimation of the E_1 (that appears as a shoulder) and overestimation of the E_2. An analogous underestimation of the E_1/E_2 ratio is observed in the literature for other zincblende semiconductors such as silicon or GaAs.[54,55] The error at the independent particle level depends on the different character of the excitations that originate the peak. As shown for ZnTe (Fig. 8) the excited electron is much more localised around the hole for the E_1 exciton than for the E_2 exciton (a similar trend is observed for the other systems). Note that while E_1 originates mainly from excitations at the high-symmetry point L, E_2 involves many one particle excitations. In fact in empirical models for the macroscopic dielectric function, the former is modelled as transitions at a two-dimensional minimum plus a bound exciton while the latter is modelled by a damped oscillator.[19,56,57]

As at the independent particle level the excited electron distribution does not depend on the hole position the error of neglecting electron-hole attraction is larger for E_1. Crystal local field effects, which are included in the RPA, affect differently the two excitations as well. They are stronger for the E_2 excitation (due to larger density inhomogeneities) and as a consequence the intensity of the corresponding peak is renormalised leading to a better E_1/E_2 ratio with respect to the independent particle approximation, though the error is still very large.

Addition of electron-hole attraction both at the Bethe-Salpeter level and through the polarisation functional dramatically improve the E_1/E_2 ratio. In particular with respect to the RPA, the polarisation functional increases the intensity of the E_1 peak, keep the intensity of E_2 unchanged (that is correct already at the RPA level). This can be understood by noticing that within the Kohn-Sham macroscopic electric field can be written as

$$\mathscr{E}^{\text{S}}(\omega) = (1-\alpha\chi(\omega))\,\mathscr{E}^{\text{tot}}(\omega) \tag{22}$$

where $\mathscr{E}^{\text{tot}} = \mathscr{E}^{\text{ind}} + \mathscr{E}^{\text{ext}}$ in Eq. 9, and we used that $\mathbf{P} = \chi\mathscr{E}^{\text{tot}}$ assuming a small $\mathscr{E}^{\text{ext}}$ so that we can consider only the first perturbation order. The first order susceptibility $\chi(\omega)$ is a complex quantity. Its imaginary part is positive for $\omega > 0$ (as it corresponds to the optical absorption), so that the sign is determined by its real part. The latter indeed is negative for energies corresponding to E_0 and E_1 (for which the polarisation functional increases the intensity) and zero or positive for energies corresponding to E_2 and E_1' (for which the polarisation functional keeps or reduces the intensity).

Besides underestimating the E_1/E_2 ratio, at the RPA (and independent particle) level the position of the E_1 and E_2 peaks is blue shifted. As shown in Fig. 9 both Bethe-Salpeter and TD-DPFT correctly redshift the peaks though to a different extent. In both cases the redshift is larger for ZnS, for which the electronic screening is smaller. The correction then decreases by increasing the chalcogen anion atomic number (thus the electronic screening). The E_2 peak is more redshifted than the E_1 peak. Within the Bethe-Salpeter—whose results better agree with the experiment—corrections are larger than within TD-DPFT. Furthermore while for the latter the corrections for E_1 and E_2 show a similar trend, at the Bethe-Salpeter level the redshift of E_2 decreases more slowly with the chalcogen anion atomic number than the redshift of the E_1.

In the analysis above we have consider only the $\alpha^{\mathrm{EMP}}\mathbf{P}$ approximation which provide the best agreement and whose results are very similar to the $\alpha^{\mathrm{CUR}}\mathbf{P}$ approximation. The JGM approximation (which is appealing as it involves the electron density rather than the static dielectric function) gives for all the studied systems poor results as the α are too large and the corrections overestimated. In fact we obtained much better results (not shown) by calculating the JGM spectra with the unshifted Kohn-Sham eigenvalues and then shift the spectra. For other systems, as those reported in the original publication,[14] we obtained good results. One explanation for those poor results can be the presence of d bands for which the jellium, even with a gap, may not be such a good model.

The general picture that emerges from the calculation of the macroscopic dielectric function is that the polarisation functionals with α modelled as a function of the dielectric constant are successful in reproducing excitonic effects in the systems here considered. Though they are not very accurate in predicting the position of the peaks they capture rather well the ratio of the intensities of the E_1 and E_2 peaks. Further modelling of approximations for the polarisation functionals should allow for more flexibility, likely by improving the energy dependent model or by including dependence of the local density.

4.2 Second Harmonic Generation

The second order susceptibility tensor $\chi^{(2)}_{ijk}(\omega_n+\omega_m;\omega_n;\omega_m)$, where ijk refers to the cartesian directions of the fields, describes how the nonlinear polarisation field $\mathbf{P}_i(\omega_n+\omega_m)$ in a direction i oscillating at a frequency $\omega_n+\omega_m$ is proportional to the product of the applied electric field components $\mathscr{E}_j(\omega_m)\mathscr{E}_k(\omega_n)$ in directions j and k oscillating at frequencies ω_n and ω_m.[60] In zincblende structures such as the bulk cubic zinc chalcogenides here studied, the only non-zero independent component of the second order susceptibility is $\chi^{(2)}_{xyz}$ for which we have calculated the module $|\chi^{(2)}|_{xyz}$ at $\omega_n=\omega_m$ (SHG).

The experimental SH intensity spectra $|\chi^{(2)}|_{xyz}$ in the 1.0-2.5 eV range[18] for cubic ZnS, ZnSe and ZnTe are plotted in the left, middle and right panels of Fig. 10. The spectrum of ZnS shows a sharp peak at about 1.85 eV corresponding to a two-photon resonance at E_0. None of the considered approximations satisfactorily reproduce the experimental spectra in this range. The TD-DFT, the $\alpha^{\mathrm{ED}}\mathbf{P}$ and the $\alpha^{\mathrm{JGM}}\mathbf{P}$ agree with the experiment for low energies. However at higher energies the intensity is strongly underestimated with respect to the experiment. The $\alpha^{\mathrm{BER}}\mathbf{P}$ functional provides a better agreement, though its intensity is still significantly smaller than experiment. We have also verified that using a broadening of 0.1 eV instead of 0.2 eV enhances the intensity of the peak, but does not change the shape of the curve. All the considered theoretical methods predict the E_0 two-photon resonance at about 1.9 eV. As discussed previously the difference in the E_0 position is mainly due to temperature effects. For ZnSe the experimental SH spectrum shows a peak at 1.35 eV (two-photon resonance at E_0) and at 2.4 eV (two-photon resonance at E_1). Similarly to ZnS, the TDDFT correctly predicts the SH intensity at low energies, but strongly underestimates the SH intensity for higher energies. The $\alpha^{\mathrm{ED}}\mathbf{P}$ result is very close to TD-DFT as the α is relatively small. Results obtained for $\alpha^{\mathrm{BER}}\mathbf{P}$ and $\alpha^{\mathrm{JGM}}\mathbf{P}$ are quite similar: they both worsen the agreement of TD-DFT at low energy and slightly improve the agreement at higher energies. The two-photon resonance at E_1 is found at about 2.6 eV in all the methods and E_0 is a weak shoulder at about 1.45 eV visible in the curves calculates with a 0.1 broadening. For ZnTe the experimental SH spectrum shows a small peak at 1.14 eV (two-photon resonance at E_0), and two larger peaks at about 1.8 eV (two-photon resonance at E_1) and at 2.0 eV (two-photon resonance at $E_1+\Delta_{\mathrm{SO}}$). As for ZnS and ZnSe $\alpha^{\mathrm{ED}}\mathbf{P}$ and $\alpha^{\mathrm{BER}}\mathbf{P}$ slightly improve the general agreement with experiment with respect to TD-DFT though it worsen the agreement at low energy. In this case the spectrum obtained with $\alpha^{\mathrm{JGM}}\mathbf{P}$ has a much larger intensity than all the other approximations and overestimate the experimental SH intensity. In JGM the two-photon resonance at E_1 is a peak at 1.85 eV, significantly redshifted with respect to the other approximations that have a shoulder at about 2.1 eV. Note that as we use scalar relativistic pseudopotentials for those calculations we cannot reproduce the spin-orbit splitting of the E_1 resonance. Results at the TD-DFT level agree closely with the calculations for the SHG imaginary part from Reshak and Auluck[23] and show reasonable agreement with other theoretical results at the independent particle level for SH intensity in the literature.[25,26]

The general performance is not very good with all approximations substantially underestimating the intensity of the experimental spectra (except for the JGM approximation in ZnTe). The underestimation of the theoretical curves is quite large even considering the error of ±20% in the absolute value of the SHG due to uncertainties in the measurement.[18] Note that the two-photon resonances at E_0 (ZnS and ZnSe) and E_1 (ZnSe and ZnTe) are enhanced in SHG because of the E^{-5} behaviour (rather than E^{-3} in the dielectric function).[26] Regarding in particular the E_0 it was argued that due to their relatively strong binding energy, excitonic effects are still important at room temperature and they are responsible of the differences observed with spectra calculated from independent particle models.[18]

No clear trend can be observed on how the PF approximations are performing with the exception of the energy dependent approximation which behaves similarly to TD-DFT with the size of the correction increasing from S to Se to Te. Differently from what we see for the macroscopic dielectric function there is no clear relation for the size of the correction due the polarisation functional either with the value of α and with the results for the macroscopic dielectric function. For example the JGM has a much larger α and it visibly over-corrects the RPA for the macroscopic dielectric function in contrast to results for the SHG of ZnS and ZnSe. We argue that the absence of a clear pattern in the functional performance is mainly due to nonlinear effects as $\alpha\mathbf{P} = \alpha\mathbf{P}^{(1)} + \alpha\mathbf{P}^{(2)} + \ldots$, thus contributing both at the laser frequency and at twice the laser frequency. In addition the SH intensity results from summing the real and imaginary part and the errors in the two parts may either cancel or sum up.

5 Conclusions

In this work we have calculated the frequency dependent macroscopic dielectric function and SHG of cubic ZnX, with X = S, Se and Te, within TD-DPFT. The latter framework, which has been described in Sec. 2, implies the approximation of both the microscopic exchange-correlation potential and the macroscopic exchange-correlation electric field as a functional of both the electronic density and the macroscopic polarisation $\mathbf{P}$. In this work we have chosen to neglect microscopic exchange-correlation effects, that are known to be unimportant for the macroscopic dielectric function of finite gap periodic crystals, and approximate the exchange-correlation electric field as $\alpha\mathbf{P}$. For α we have used expressions that have been proposed in the recent literature and listed in Sec. 2. Results were compared with the available experimental data, and with theoretical results at the independent particle and RPA level and when feasible with results obtained from the solution of the Bethe-Salpeter equation.

For the macroscopic dielectric function (Sec. 4.1) we have found that, with respect to results obtained within the RPA, the polarisation functionals with α approximated as a function of the static macroscopic dielectric function improve the agreement with the experimental results though differences are still visible especially in the peaks position. The agreement with the experimental curves is not as good as that obtained within the Bethe-Salpeter equation framework, on the other hand the latter approach is computationally much more expensive. In fact for the polarisation functionals considered here the additional computational cost with respect to a RPA or standard TD-DFT calculation is negligible while they allow in principle to capture long-range correlation. It is then certainly of interest to further develop approximations for the polarisation functionals and the interest is not restricted to Solid State systems. For example in long (though finite) molecular chains it has been shown that the exact exchange-correlation potential counteracts the applied electric field.[61] The effect is captured, at least partially, by orbital dependent approximations[62–64] or within current-density functional theory[65] that can be however awkward to implement. Functionals containing polarisation (that for finite systems are functionals of the electric density alone) may be employed instead to mimic the counteracting component of the exchange-correlation potential in a simpler and more efficient way.

For the SHG we did not obtain a clear picture of the performance of the polarisation functionals. They tend to increase the SH intensity that is strongly underestimated within TD-DFT. However in general the intensity is still significantly underestimated and in addition the agreement at low photon energies (static limit) is worsened with respect to TD-DFT.

6 Acknowledgements

M. G. dedicates this work to Evert Jan Baerends. She also acknowledges discussions with the participants in the E.J. Baerends Symposium. C. A. acknowledges EUSpec Cost Action MP1306. This work used the computing facilities of the Atomistic Simulation Centre–Queen's University Belfast, the one of CINaM Aix-Marseille Université. Computing time has been provided as well by the "Curie" national GENGI-IDRIS supercomputing center under contract No. x2012096655. C. A. thanks A. Zappelli for the efficient maintenance of the Pancho cluster.

References

1 G. Onida, L. Reining, and A. Rubio, *Rev. Mod. Phys.*, 2002, **74**(2), 601–659.
2 G. Strinati, *Riv. Nuovo Cimento*, 1988, **11**(12), 1–86.
3 P. Abbamonte, T. Graber, J. P. Reed, S. Smadici, C.-L. Yeh, A. Shukla, J.-P. Rueff, and W. Ku, *Proceedings of the National Academy of Sciences*, 2008, **105**(34), 12159–12163.
4 Note that the density response $\chi^{\rho\rho}$ and L are strictly related: χ can be derived from L by taking the trace.
5 We do not include in the present analysis kernels derived from hybrid functionals. Those kernels contain a long-range Hartree-Fock part "screened" by the empirical mixing parameter which can be considered an approximation of the of the BS kernel.
6 Standard approximations for the exchange-correlation kernel not only fail to capture the excitonic effects of optical spectra of semiconductors and insulators, but they also severely underestimate the spectrum offset. In this work we cure the latter shortcoming by introducing a material dependent scissor operator (see discussion in Sec. 3).
7 A. Marini, R. Del Sole, and A. Rubio, *Phys. Rev. Lett.*, 2003, **91**, 256402.

8 F. Sottile, V. Olevano, and L. Reining, *Phys. Rev. Lett.*, 2003, **91**, 056402.

9 L. Reining, V. Olevano, A. Rubio, and G. Onida, *Phys. Rev. Lett.*, 2002, **88**, 066404.

10 S. Botti, F. Sottile, N. Vast, V. Olevano, L. Reining, H.-C. Weissker, A. Rubio, G. Onida, R. Del Sole, and R. Godby, *Physical Review B*, 2004, **69**(15), 155112.

11 S. Botti, A. Fourreau, F. m. c. Nguyen, Y.-O. Renault, F. Sottile, and L. Reining, *Phys. Rev. B*, 2005, **72**, 125203.

12 S. Sharma, J. K. Dewhurst, A. Sanna, and E. K. U. Gross, *Phys. Rev. Lett.*, 2011, **107**, 186401.

13 S. Rigamonti, S. Botti, V. Veniard, C. Draxl, L. Reining, and F. Sottile, *Phys. Rev. Lett.*, 2015, **114**, 146402.

14 P. E. Trevisanutto, A. Terentjevs, L. A. Constantin, V. Olevano, and F. Della Sala, *Physical Review B*, 2013, **87**(20), 205143.

15 W. G. Aulbur, L. Jönsson, and J. W. Wilkins, *Physical Review B*, 1996, **54**(12), 8540.

16 P. L. de Boeij, F. Kootstra, J. A. Berger, R. van Leeuwen, and J. G. Snijders, *The Journal of Chemical Physics*, 2001, **115**(5), 1995–1999.

17 J. A. Berger, *Phys. Rev. Lett.*, 2015, **115**, 137402.

18 H. P. Wagner, M. Kühnelt, W. Langbein, and J. M. Hvam, *Phys. Rev. B*, 1998, **58**, 10494–10501.

19 T. Tsuchiya, S. Ozaki, and S. Adachi, *Journal of Physics: Condensed Matter*, 2003, **15**(22), 3717.

20 in *Handbook on Physical Properties of Semiconductors;* Springer US, 2004; pp. 123–160.

21 in *Handbook on Physical Properties of Semiconductors;* Springer US, 2004; pp. 211–253.

22 in *Handbook on Physical Properties of Semiconductors;* Springer US, 2004; pp. 161–210.

23 A. H. Reshak and S. Auluck, *Physica B: Condensed Matter*, 2007, **388**(12), 34 – 42.

24 M.-Z. Huang and W. Y. Ching, *Phys. Rev. B*, 1993, **47**, 9449–9463.

25 M.-Z. Huang and W. Y. Ching, *Phys. Rev. B*, 1993, **47**, 9464–9478.

26 E. Ghahramani, D. J. Moss, and J. E. Sipe, *Phys. Rev. B*, 1991, **43**, 9700–9710.

27 Z. Nourbakhsh, *Journal of Alloys and Compounds*, 2010, **505**(2), 698–711.

28 R. Khenata, A. Bouhemadou, M. Sahnoun, A. H. Reshak, H. Baltache, and M. Rabah, *Computational Materials Science*, 2006, **38**(1), 29–38.

29 J. L. P. Hughes and J. E. Sipe, *Phys. Rev. B*, 1998, **58**, 7761–7767.

30 S. Z. Karazhanov, P. Ravindran, A. Kjekshus, H. Fjellvåg, and B. G. Svensson, *Phys. Rev. B*, 2007, **75**, 155104.

31 X. Gonze, P. Ghosez, and R. Godby, *Physical Review Letters*, 1995, **74**(20), 4035–4038.

32 R. Resta, *Physical Review Letters*, 1996, **77**(11), 2265–2267.

33 D. Vanderbilt, *Physical Review Letters*, 1997, **79**(20), 3966–3969.

34 R. Martin and G. Ortiz, *Physical Review B*, 1997, **56**(3), 1124–1140.

35 N. T. Maitra, I. Souza, and K. Burke, *Physical Review B*, 2003, **68**(4), 045109.

36 S. K. Ghosh and A. K. Dhara, *Phys. Rev. A*, 1988, **38**, 1149–1158.

37 We work here in the length gauge which is derived by the multipolar gauge in the electric dipole approximation and is routinely used in the calculation of optical properties in periodic systems.

38 M. Corradini, R. Del Sole, G. Onida, and M. Palummo, *Phys. Rev. B*, 1998, **57**, 14569–14571.

39 A. Marini, C. Hogan, M. Grüning, and D. Varsano, *Comp. Phys. Comm.*, 2009, **180**, 1392.

40 J. A. Berger, P. L. de Boeij, and R. van Leeuwen, *Phys. Rev. B*, 2007, **75**, 035116.

41 C. Attaccalite and M. Grüning, *Physical Review B*, 2013, **88**(23), 235113.

42 I. Souza, J. Íñiguez, and D. Vanderbilt, *Phys. Rev. B*, 2004, **69**, 085106.

43 R. W. Nunes and X. Gonze, *Phys. Rev. B*, 2001, **63**, 155107.

44 J. Crank and P. Nicolson In *Mathematical Proceedings of the Cambridge Philosophical Society*, Vol. 43, pp. 50–67. Cambridge Univ Press, 1947.

45 J. P. Perdew, K. Burke, and M. Ernzerhof, *Phys. Rev. Lett.*, 1996, **77**, 3865–3868.

46 P. G. et al., *J. Phys. Condens. Matter*, 2009, **21**, 395502.

47 N. Troullier and J. L. Martins, *Phys. Rev. B*, 1991, **43**, 1993–2006.

48 Notes on pseudopotential generation. P. Giannozzi; http://www.quantum-espresso.org/wp-content/uploads/Doc/pseudo-gen/, 2015.

49 A. D. Corso, *Computational Materials Science*, 2014, **95**, 337 – 350.

50 H. J. Monkhorst and J. D. Pack, *Phys. Rev. B*, 1976, **13**, 5188–5192.

51 D. Kammerlander, S. Botti, M. A. L. Marques, A. Marini, and C. Attaccalite, *Phys. Rev. B*, 2012, **86**, 125203.

52 As discussed excitonic effects (electron-hole attraction) are responsible for most of the differences observed between experimental and the theoretical spectra, but there are other factors that may contribute significantly. First, the spectrum has been measured at room temperature while no temperature effects has been included in the cal-

culations, except for the empirical Lorentzian broadening. Experimental studies on temperature effects in ZnS, ZnSe and ZnTe[20–22] show that the absorption edge is redshifted by about 0.1 eV at room temperature. In principle these effects can be included by means of a finite temperature molecular dynamics or within many-body perturbation theory in the electron-phonon coupling,[66] but this is beyond the scope of the present work. Second, the KS electronic structure—even if corrected for the band gap problem—may still introduce errors in the peak position. In particular for those systems standard DFT approximations underbind d-bands by about 2-3 eV and because of artificial $p-d$ hybridisation may induce significant errors in the valence top bands. We observe indeed that the d bands are at too high energy. We also found different values for the energy of the top valence band at X and L (-2.26 eV and -0.89 eV) with respect to the values reported by Zakharov et al.[67] (-2.06 eV and -0.78 eV). On the other hand we have checked that even correcting the position of the d bands by adding a Hubbard U does not change substantially the position of the X and L critical points. Yet another source of error may be the use of the experimental rather than the theoretical lattice parameter which effectively corresponds to slightly strain the systems. Strain may modify the electronic structure and as a consequence the optical spectra[27,28] even if the work of Karazhanov and coworkers[30] suggests that those effects are neglible when using the experimental rather than theoretical lattice constant in bulk zinc chalcogenides.

53 In fact different calculations choose different scissor operators. Note that this is a parameter, not an output of the calculation. We have compared our spectra with the spectra from Ghahramani and coworkers [26] ,Huang and coworkers[24] and Reshak and Auluck[23].

54 W. Hanke and L. J. Sham, Jul , 1979, **43**, 387–390.

55 W. Hanke and L. J. Sham, May , 1980, **21**, 4656–4673.

56 S. Adachi and T. Taguchi, *Phys. Rev. B*, 1991, **43**, 9569–9577.

57 K. Sato and S. Adachi, *Journal of Applied Physics*, 1993, **73**(2), 926–931.

58 K. Momma and F. Izumi, *J. Appl. Crystallogr.*, 2011, **44**, 1272–1276.

59 Experimental optical absorption spectra are taken from Ref.[30] that took data tabulated in ”Optical Constants of Crystalline and Amorphous Semiconductors: Numerical Data and Graphical Information”, edited by S. Adachi (Kluwer Academic, Boston, 1999).

60 R. W. Boyd in *Nonlinear Optics (Third Edition)*, ed. R. W. Boyd; Academic Press, Burlington, third edition ed., 2008; pp. 1 – 67.

61 S. J. A. van Gisbergen, P. R. T. Schipper, O. V. Gritsenko, E. J. Baerends, J. G. Snijders, B. Champagne, and B. Kirtman, *Phys. Rev. Lett.*, 1999, **83**, 694–697.

62 C. D. Pemmaraju, S. Sanvito, and K. Burke, *Phys. Rev. B*, 2008, **77**, 121204.

63 M. Gruning, O. V. Gritsenko, and E. J. Baerends, *The Journal of Chemical Physics*, 2002, **116**(15), 6435.

64 O. V. Gritsenko, S. J. A. van Gisbergen, P. R. T. Schipper, and E. J. Baerends, *Phys. Rev. A*, 2000, **62**, 012507.

65 M. van Faassen, P. L. de Boeij, R. van Leeuwen, J. A. Berger, and J. G. Snijders, *Phys. Rev. Lett.*, 2002, **88**, 186401.

66 A. Marini, *Phys. Rev. Lett.*, 2008, **101**, 106405.

67 O. Zakharov, A. Rubio, X. Blase, M. L. Cohen, and S. G. Louie, *Phys. Rev. B*, 1994, **50**, 10780–10787.

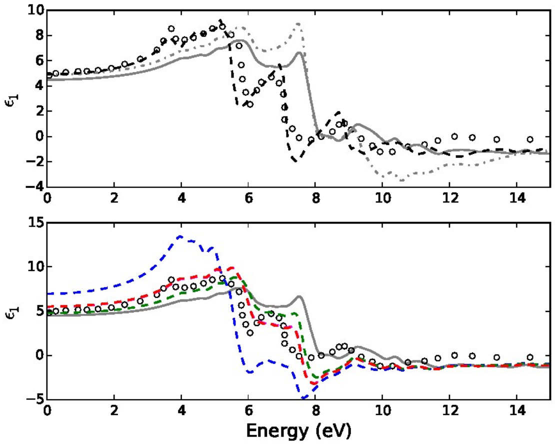

Fig. 2 Real part of the macroscopic dielectric function ε_1 of bulk ZnS. Top panel: experimental spectrum[20](circles) compared with the independent particle (grey dashed-dotted line), random phase approximation (grey continuous line) and Bethe-Salpeter equation (black dashed line). Bottom panel: experimental spectrum (circles) compared with the approximations for the polarisation functional described in Sec. 2, $\alpha^{\rm EMP}\mathbf{P}$ (red dashed line), $\alpha^{\rm BER}\mathbf{P}$ (magenta dashed line), $\alpha^{\rm ED}\mathbf{P}$ (green dashed line) and $\alpha^{\rm JGM}\mathbf{P}$ (blue dashed line). For reference the random phase approximation is also shown (grey continuous line).

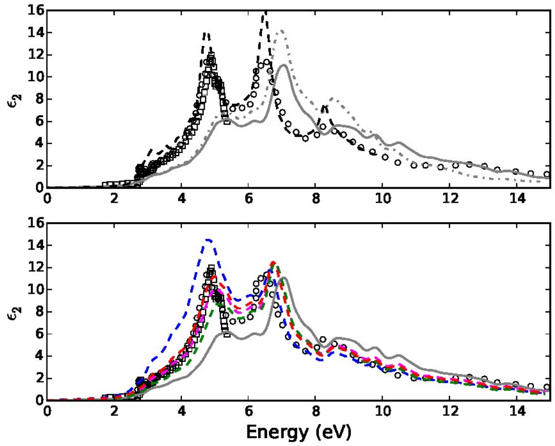

Fig. 3 Optical absorption (imaginary part of the macroscopic dielectric function ε_2) in bulk ZnSe. Top panel: experimental spectrum at room temperature[21](circles) and at 20K[21](squares) are compared with the independent particle (grey dashed-dotted line), random phase approximation (grey continuous line) and Bethe-Salpeter equation (black dashed line). Bottom panel: experimental spectra (circles and) are compared with the approximations for the polarisation functional described in Sec. 2, $\mathscr{E}^{\rm xc} \approx \alpha^{\rm EMP}\mathbf{P}$ (red dashed line), $\mathscr{E}^{\rm xc} \approx \alpha^{\rm BER}\mathbf{P}$ (magenta dashed line), $\mathscr{E}^{\rm xc} \approx \alpha^{\rm ED}\mathbf{P}$ (green dashed line) and $\mathscr{E}^{\rm xc} \approx \alpha^{\rm JGM}\mathbf{P}$ (blue dashed line). For reference the random phase approximation is also shown (grey continuous line).

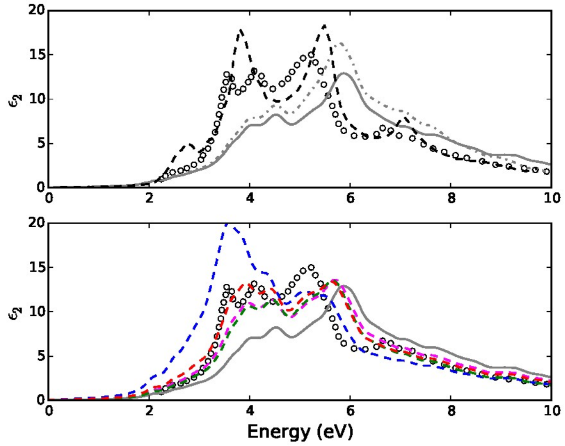

Fig. 4 Optical absorption (imaginary part of the macroscopic dielectric function ε_2) in bulk ZnTe. Top panel: experimental spectrum[22](circles) compared with the independent particle (grey dashed-dotted line), random phase approximation (grey continuous line) and Bethe-Salpeter equation (black dashed line). Bottom panel: experimental spectrum (circles) compared with the approximations for the polarisation functional described in Sec. 2, $\mathscr{E}^{\rm xc} \approx \alpha^{\rm EMP}\mathbf{P}$ (red dashed line), $\mathscr{E}^{\rm xc} \approx \alpha^{\rm BER}\mathbf{P}$ (magenta dashed line), $\mathscr{E}^{\rm xc} \approx \alpha^{\rm ED}\mathbf{P}$ (green dashed line) and $\mathscr{E}^{\rm xc} \approx \alpha^{\rm JGM}\mathbf{P}$ (blue dashed line). For reference the random phase approximation is also shown (grey continuous line).

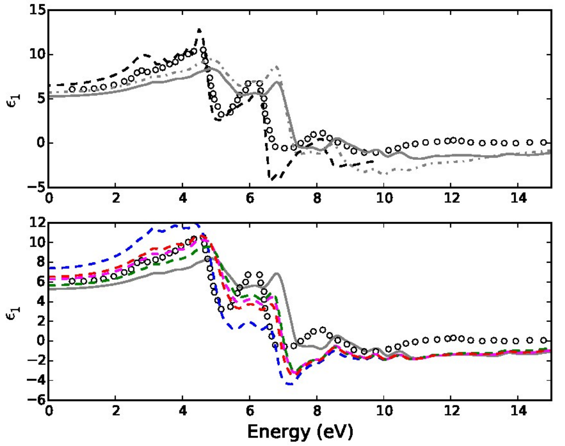

Fig. 5 Real part of the macroscopic dielectric function ε_1 of bulk ZnSe. Top panel: experimental spectrum[20](circles) compared with the independent particle (grey dashed-dotted line) and random phase approximation (grey continuous line) and Bethe-Salpeter equation (black dashed line). Bottom panel: experimental spectrum (circles) compared with the approximations for the polarisation functional described in Sec. 2, $\alpha^{\rm EMP}\mathbf{P}$ (red dashed line), $\alpha^{\rm BER}\mathbf{P}$ (magenta dashed line), $\alpha^{\rm ED}\mathbf{P}$ (green dashed line) and $\alpha^{\rm JGM}\mathbf{P}$ (blue dashed line). For reference the random phase approximation is also shown (grey continuous line).

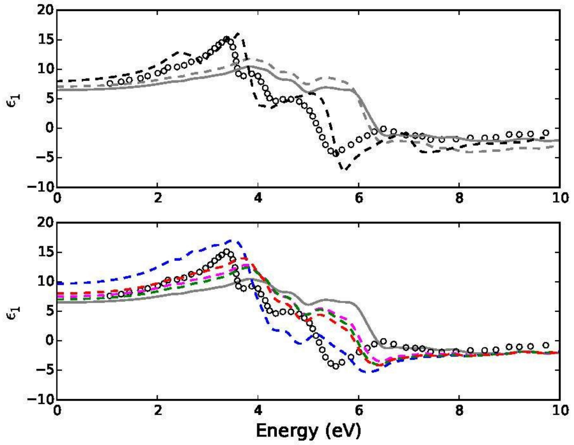

Fig. 6 Real part of the macroscopic dielectric function ε_1 of bulk ZnTe. Top panel: experimental spectrum[22](circles) compared with the independent particle (grey dashed-dotted line) and random phase approximation (grey continuous line) and Bethe-Salpeter equation (black dashed line). Bottom panel: experimental spectrum (circles) compared with the approximations for the polarisation functional described in Sec. 2, $\mathscr{E}^{\mathrm{xc}} \approx \alpha^{\mathrm{EMP}}\mathbf{P}$ (red dashed line), $\mathscr{E}^{\mathrm{xc}} \approx \alpha^{\mathrm{BER}}\mathbf{P}$ (magenta dashed line), $\mathscr{E}^{\mathrm{xc}} \approx \alpha^{\mathrm{ED}}\mathbf{P}$ (green dashed line) and $\mathscr{E}^{\mathrm{xc}} \approx \alpha^{\mathrm{JGM}}\mathbf{P}$ (blue dashed line). For reference the random phase approximation is also shown (grey continuous line).

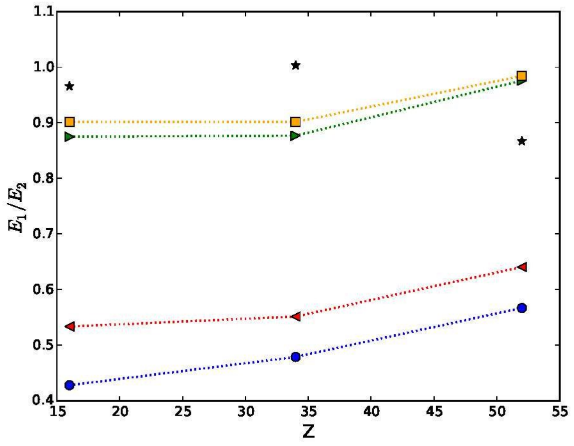

Fig. 7 E_1/E_2 ratio of peak intensities in ε_2 as a function of the chalcogen anion atomic number Z in calculations at Bethe-Salpeter (yellow squares), TD-DPFT with the $\alpha^{\mathrm{EMP}}\mathbf{P}$ functional (green right triangles), RPA (red left triangles) and independent particle (blue circles) level. Experimental ratios are reported for comparison (black stars). Lines between points are a guide for the eye.

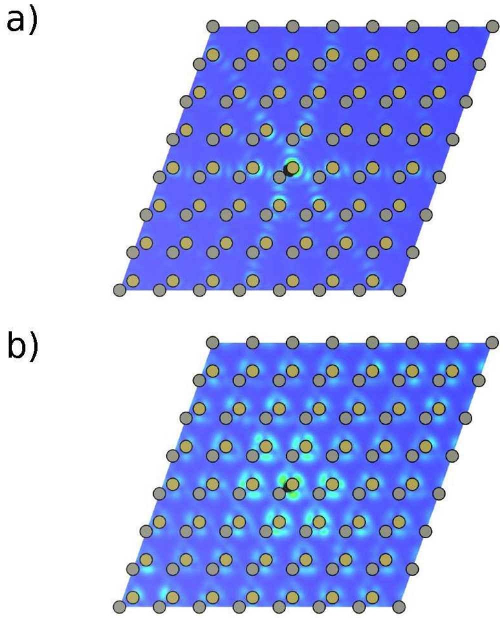

Fig. 8 Slice of the excitonic wavefunction in ZnTe for a) the strongest exciton that contributes to the E_1 peak and b) the strongest exciton that contributes to the E_2 peak. View along one of the lattice vectors of $7 \times 7 \times 7$ unit cells of cubic ZnTe (Zn atoms are in grey, Te atoms in olive green). The hole position is represented by a dummy atom (black) and coincides with the position of the Te in one of the unit cells. The 100 lattice plane passing through the hole position slices the excited electron wavefunction (dark blue correspond to no excited electronic density). Plots have been rendered using VESTA.[58]

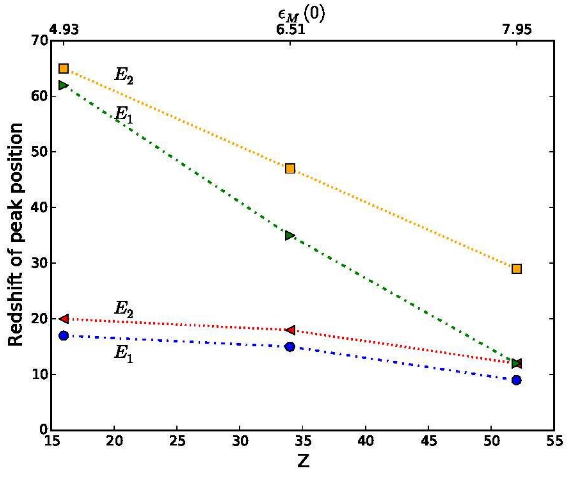

Fig. 9 Redshift with respect the RPA results of the E_1 and E_2 peaks position in ε_2 as a function of the chalcogen anion atomic number Z (and of the static macroscopic dielectric constant $\varepsilon_M(0)$ within the Bethe-Salpeter equation framework) for the Bethe-Salpeter equation (orange squares, E_2, and green right triangles, E_1) and the polarisation functional with α^{EMP} (red left triangles, E_2, and blue circles, E_1). Lines between points are a guide for the eye.

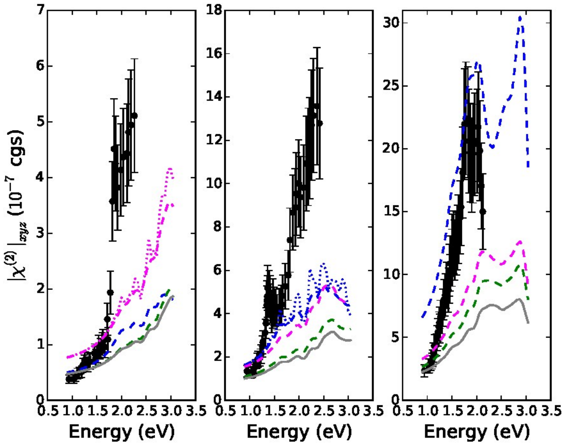

Fig. 10 SHG of bulk cubic ZnS (left), ZnSe (middle) and ZnTe (right). The experimental spectrum[18,59] (circles + error bar of 20% on absolute intensity) are compared with the time-dependent density functional theory results obtained with the PBE functional (grey continuous line) and with the approximations for the polarisation functional described in Sec. 2, $\mathscr{E}^{\rm xc} \approx \alpha^{\rm BER}\mathbf{P}$ (magenta dashed line), $\mathscr{E}^{\rm xc} \approx \alpha^{\rm ED}\mathbf{P}$ (green dashed line) and $\mathscr{E}^{\rm xc} \approx \alpha^{\rm JGM}\mathbf{P}$ (blue dashed line). For comparison the $\mathscr{E}^{\rm xc} \approx \alpha^{\rm BER}\mathbf{P}$ (magenta dotted line) and $\mathscr{E}^{\rm xc} \approx \alpha^{\rm JGM}\mathbf{P}$ (blue dotted line) have been calculated with a Lorentzian broadening of 0.1 eV respectively for ZnS and ZnSe.